

Supramolecular heterostructures formed by sequential epitaxial deposition of two-dimensional hydrogen-bonded arrays

Vladimir V. Korolkov¹, Matteo Baldoni², Kenji Watanabe³, Takashi Taniguchi³, Elena Besley^{2*} and Peter H. Beton^{1*}

Two-dimensional (2D) supramolecular arrays provide a route to the spatial control of the chemical functionality of a surface, but their deposition is in almost all cases limited to a monolayer termination. Here we investigated the sequential deposition of one 2D array on another to form a supramolecular heterostructure and realize the growth—normal to the underlying substrate—of distinct ordered layers, each of which is stabilized by in-plane hydrogen bonding. For heterostructures formed by depositing terephthalic acid or trimesic acid on cyanuric acid/melamine, we have determined, using atomic force microscopy under ambient conditions, a clear epitaxial arrangement despite the intrinsically distinct symmetries and/or lattice constants of each layer. Structures calculated using classical molecular dynamics are in excellent agreement with the orientation, registry and dimensions of the epitaxial layers. Calculations confirm that van der Waals interactions provide the dominant contribution to the adsorption energy and registry of the layers.

The formation of two-dimensional (2D) supramolecular arrays provides a highly flexible route to the control of the spatial organization, down to the molecular scale, of the chemical functionality of a surface^{1–4}. These molecular networks, which can be formed through self-assembly processes on a variety of different substrates, including semiconductors^{5,6}, metals^{7,8}, insulators^{9–11} and layered materials^{12–15}, are, in almost all cases, limited to monolayer thickness. Progress towards the growth of higher layers has so far been much more limited, with demonstrations of bilayer growth^{16,17} and site-specific molecular adsorption^{5,18–24}. Specifically, the additional functional control, which may be achieved through the formation of heterostructures realized by placing one supramolecular layer on another to result in growth into the third dimension perpendicular to the substrate, has not been widely explored for these materials. Such an additional control of material properties is well established for semiconductors, both organic^{25–30} and inorganic³¹, and, more recently, for layered materials³², which provides a strong motivation to explore analogue materials derived from stacked supramolecular networks. Here we describe the successful formation of heterostructures formed by the sequential growth of distinct 1D and 2D arrays. It is possible, using high-resolution atomic force microscopy (AFM), to determine an epitaxial alignment between successive layers. Furthermore, we demonstrate using classical molecular dynamics (MD) simulations that the placement and dimensions of the layers may be predicted using well-established force fields.

We chose to investigate a combination of a bicomponent hexagonal network (CAM) formed by cyanuric acid (CA) and melamine (M), and monocomponent honeycomb and linear arrays formed by, respectively, trimesic acid (TMA) and terephthalic acid (TPA). The heterostructures are formed by first depositing a CAM monolayer that is then used as the substrate for a further deposition cycle whereby monolayers of TMA or TPA are adsorbed to form a heterostructure. The layers are deposited via sequential immersion

in solutions, and we have investigated heterostructure formation on the surface of hexagonal boron nitride (hBN) flakes that are exfoliated from millimetre-scale crystals; we have recently demonstrated that these substrates support molecular self-assembly^{13,14}. As both hBN and, potentially, the supramolecular heterostructures are insulating, we use AFM to acquire images of the molecular arrangements in adsorbed networks. This work represents an advance in the application of AFM to imaging such networks through the acquisition of images, under ambient conditions, with sufficiently high resolution to identify the relative placement of molecules in different layers of the resulting heterostructures.

The hBN substrates typically have thicknesses of a few tens of nanometres and lateral dimensions of several tens of micrometres. Flakes are transferred to a SiO₂/Si substrate and, after cleaning, molecular layers are deposited by immersion in either aqueous solutions of CA and melamine, or ethanolic solutions of TMA or TPA. All the images were acquired under ambient conditions using an Asylum Cypher AFM (full details of the substrate and sample preparation are provided in Methods).

Results and discussion

CAM on hBN. AFM images of the CAM network adsorbed on hBN reveal a honeycomb array (Fig. 1) very similar to that previously observed in scanning tunnelling microscopy studies of CAM on semiconductors³³, graphite³⁴ and metals^{35,36}. On hBN, the array has a period of $a_{\text{CAM}} = 0.98 \pm 0.02$ nm, and is most clearly observed in high-resolution AFM images acquired in the tapping mode using the third harmonic resonant frequency of the cantilever (Fig. 1a), in which six topographically bright features are distributed around the hexagonal unit cell. The images are consistent with the optimized structure of CAM on hBN predicted by MD calculations (Fig. 1b), in which junctions between CA and melamine are each stabilized by three hydrogen bonds (more details below). The adsorbed CAM layers are, within

¹School of Physics & Astronomy, University of Nottingham, Nottingham NG7 2RD, UK. ²School of Chemistry, University of Nottingham, Nottingham NG7 2RD, UK. ³National Institute for Materials Science, 1-1 Namiki, Tsukuba, Ibaraki 305-0044, Japan.

*e-mail: elena.besley@nottingham.ac.uk; peter.beton@nottingham.ac.uk

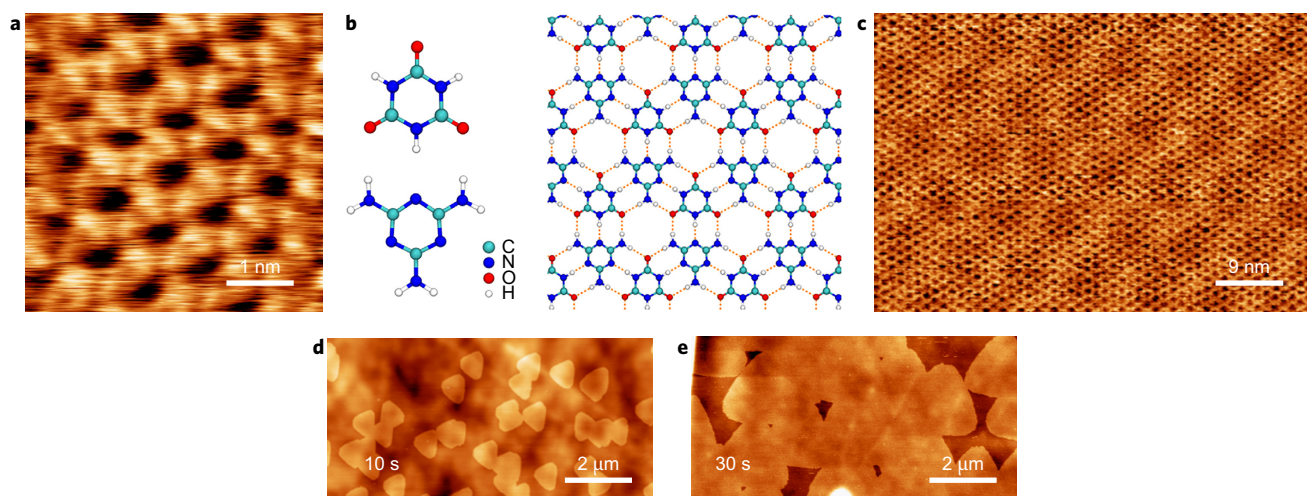


Figure 1 | Adsorption of CAM on hBN. **a**, The tapping mode image acquired using a third harmonic resonance shows the honeycomb CAM network with a period of 0.98 ± 0.02 nm. **b**, Fully optimized molecular structures of CA (upper left), melamine (lower left) and the CAM honeycomb arrangement, which is stabilized by three hydrogen bonds between neighbouring molecules (shown as dashed red lines). **c**, AFM image showing a moiré pattern with a period of 6.5 ± 0.4 nm formed by CAM on hBN—the angle between the principal axes of the CAM and the moiré pattern is $21 \pm 1^\circ$. **d,e**, Large-area images show the variation in coverage and island size for different immersion times of 10 s (**d**) and 30 s (**e**).

experimental error, structurally identical to layers of the supramolecular crystal melamine–cyanurate, which has a lattice constant of 0.96 nm (ref. 37).

In intermediate-resolution images (Fig. 1c), the molecular network coexists with a moiré pattern, which has a period of 6.5 ± 0.4 nm and subtends an angle of $21 \pm 1^\circ$ with the lattice vectors of the CAM honeycomb. The observation of a misaligned moiré pattern implies that the CAM network is rotated with respect to the substrate. This is confirmed by contact-mode AFM images (Supplementary Fig. 1), in which the hBN lattice may be resolved to show a misalignment of $3 \pm 1^\circ$ between the hBN and CAM symmetry axes.

By varying the immersion time of the sample, it is possible to control the surface coverage; larger-area images show micrometre-scale triangular islands of CAM on the surface (Fig. 1d,e) with dimensions that increase with immersion time. This can be adjusted to a near-monolayer coverage and it is also possible to form second layers, multilayers and even nanocrystals by increasing the immersion time, by repetition of immersion cycles or by increasing the concentration of the solution (Supplementary Fig. 2). The large, micrometre-scale crystallites in Fig. 1 provide the substrate for further layers of material.

CAM/TMA heterostructures. To explore the heterostructure formation we deposited TMA on the CAM-terminated hBN. As shown in Fig. 2, TMA forms a honeycomb arrangement with domains of dimensions greater than 100 nm and a period of $a_{\text{TMA}} = 1.7 \pm 0.1$ nm. The TMA arrays have a unique alignment, and images, in which both the CAM and TMA are resolved (Fig. 2b), show that the TMA axes are rotated by 30° relative to the CAM. The TMA arrays have a monolayer thickness (profile heights in Fig. 2c) and are structurally identical to the ‘chicken-wire’ arrangement identified by Griessl *et al.*³⁸ (as shown in Fig. 2d). With the near coincidence of the TMA lattice period with $\sqrt{3}a_{\text{CAM}}$, we identify this arrangement as a $(\sqrt{3} \times \sqrt{3})R30^\circ$ phase relative to the CAM layer on which it is overlaid. The coverage of TMA can also be controlled by immersion time (large-area images are included in Supplementary Fig. 3).

The observation that arrays of TMA have a very precise epitaxial relationship with the underlying CAM network implies that the energetics of adsorption must be anisotropic and drive a specific

registration. However, the interlayer interactions are expected to be dominated by van der Waals forces and to the first order might be expected to be only weakly anisotropic. To explore the energetics of epitaxial growth, classical MD simulations were performed using the LAMMPS simulation package³⁹. The OPLS potential^{40,41}, which was previously used to model the self-assembly of CA molecules⁴² and molecular adsorption on 2D materials⁴³, was employed with additional parameters derived for CA and melamine using density functional theory as implemented in the CP2K program package⁴⁴. The full computational details are included in Supplementary Information.

The interaction of CA and melamine adsorbed on a model hBN surface was investigated computationally; hBN was treated as a rigid substrate, using Lennard–Jones potential with parameters taken from Lee⁴⁵ and with atoms fixed at their crystallographic positions. A layer of alternating CA and melamine molecules with a hexagonal motif was placed on top of hBN and equilibrated using MD. The predicted period of 0.975 nm is in excellent agreement with experiment (full details of static and dynamical simulations are included in Supplementary Information). The energetics of ensembles at different orientations relative to the model CAM substrate suggest that, in agreement with experiment, there is a reduction in energy for rotations of $\pm 2^\circ$, although the energy change is small, less than kT (where k is the Boltzmann constant and T is the temperature) per molecule.

To determine the energetics that drive the epitaxial alignment we overlaid a rigid layer of TMA as optimized in vacuum on a rigid CAM layer; the calculated lattice constant of the gas-phase TMA, 1.69 nm, is almost exactly equal to the CAM lattice constant multiplied by $\sqrt{3}$. By varying the relative orientation and position of the rigid TMA and CAM layers, we calculated the energy landscape that corresponded to the adsorbed layer; a full TMA structure relaxation was then performed to ensure that the calculated energy minima represented locally stable configurations. The minimum energy orientation of the TMA was readily confirmed as 30° relative to the CAM (Supplementary Information gives further details). The energy of the TMA layer in this orientation for different placement registry was also calculated and the results are shown in Fig. 3. In short, we find energy minima when TMA molecules are placed directly above either the CA or the melamine molecules (Fig. 3b,c, respectively); owing to the commensurability of the lattices, in this

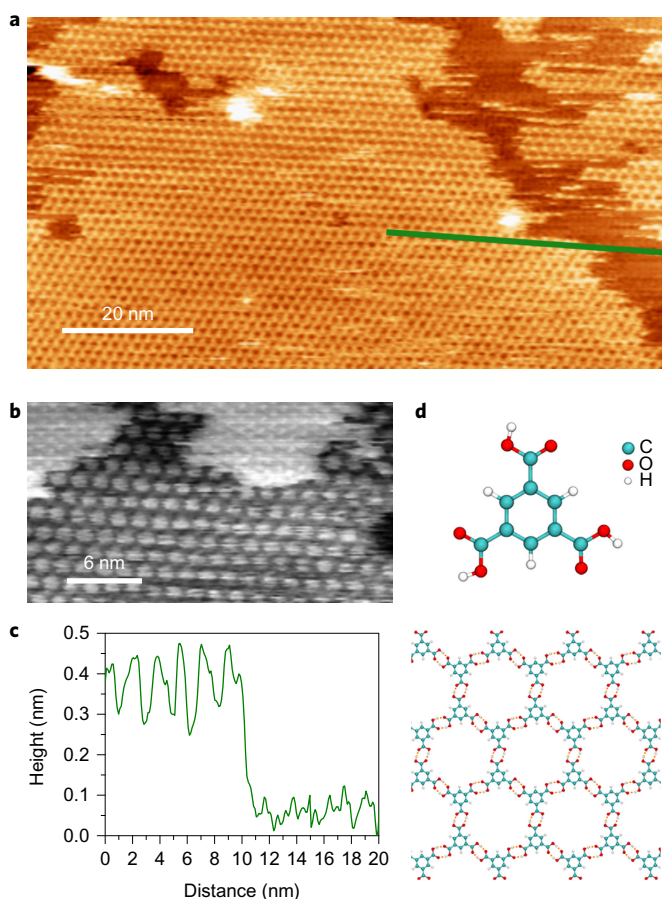


Figure 2 | Heterostructures of CAM and TMA. **a**, The large-area AFM image shows a honeycomb ('chicken-wire') arrangement of TMA (bright contrast) on CAM (dark contrast). **b**, Higher-resolution image in reverse contrast chosen to highlight the alignment between TMA (lower part) and CAM (the array in the brighter regions in the upper part of the image). The principal axes of TMA are rotated relative to CAM by 30°. **c**, The profile along the green line in **a** shows a height of ~ 0.35 nm of the TMA layer. **d**, Fully optimized molecular structures of TMA and the honeycomb TMA network.

orientation all the TMA molecules reside above equivalent sites in the CAM layer. The energy plot in Fig. 3 also shows an energy maximum when the TMA sits above a 'pore' in the CAM layer (that is, at the centre of the hexagonal motif of CAM). The maximum adsorption energy is calculated to be 0.79 eV per molecule and the energy barrier in moving TMA to the most unfavourable position is approximately 0.1 eV per molecule. The total interaction energy may be decomposed into van der Waals and Coulombic contributions, and we find (Fig. 3) that the dominant contribution ($\sim 90\%$) to the adsorption energy comes from the van der Waals term. The energy maximum above a pore may be understood as a reduced interlayer van der Waals interaction when molecules in one layer are placed over voids in the lower layer, or, effectively, a drive towards interlayer close packing.

Full MD simulations, in the which both the CAM and TMA layers were flexible and allowed to move (Supplementary Figs 9 and 10), confirm that the minima identified in Fig. 3 are stable, and we find that the lowest energy occurs for TMA above melamine. Although we cannot distinguish CA and melamine molecules in our AFM images, we were able to determine experimentally that the pores of the TMA and CAM are offset and are not coincident (and thus rules out the registry in Fig. 3d), which is consistent with our MD calculations (Supplementary Fig. 4 gives additional

images and details). Thus, the calculated structures are in excellent agreement with the dimensions, orientation and registry observed for epitaxial TMA.

CAM/TPA heterostructures. We also investigated the solution deposition of TPA by immersion in an ethanolic solution. This results in the formation of highly anisotropic islands with typical lengths and widths of 300 and 50 nm, respectively (Fig. 4a). Line profiles show that the islands have a height of approximately 0.3 nm (Fig. 4a inset), consistent with a flat-lying aromatic molecule. In phase images (Fig. 4b), the rows, the background CAM array (hexagonal array at the edges of Fig. 4b) and the CAM/hBN moiré pattern (contrast bands at the edge of Fig. 4b) are all resolved. In addition, we observe bright lines that run along the 1D islands, which are spaced by approximately 3.5 nm and correspond to an additional moiré pattern at the TPA/CAM interface.

The structure of TPA and the hydrogen-bonding junction, which results in the formation of 1D rows, is shown in Fig. 4e. From Fig. 4b it is possible to determine that the 1D rows within the TPA islands run parallel to one of the principal axes of CAM. This is observed more clearly in contact-mode AFM images (Fig. 4c,d); these show sequential images that are acquired as the deflection (that is, force) set point is gradually increased. At a low set point (Fig. 4d), the molecular resolution images of the TPA array show a separation along the rows of $a_{\text{TPA}} = 1.00 \pm 0.02$ nm. At a higher set point (Fig. 4c), the increased tip-molecule forces result in a local removal of the TPA layer, and the underlying CAM network is resolved.

The overlay of images (Fig. 4c,d) confirms the alignment of TPA and CAM. Moreover, there is a commensurate arrangement that arises from the separation of neighbouring rows; we find that three TPA rows are accommodated in two rows of the CAM lattice, and correspond to a distance of $\sqrt{3}a_{\text{CAM}} = 1.7 \pm 0.1$ nm, to give a row separation of $a_{\text{CAM}}/\sqrt{3} = 0.57 \pm 0.05$ nm. These images also show the relative positions of TPA molecules in neighbouring rows; as shown in Fig. 4e, the displacement corresponds to one-half of the period parallel to the row and the lattice vectors marked in Fig. 4e are $a_{\text{CAM}}(1/\sqrt{3}, \pm 1/2)$. Consequently, TPA molecules in every sixth row are positioned above an equivalent site in the underlying CAM and give rise to the observed interlayer moiré pattern (every other row, and specifically every third row, of TPA is displaced parallel to the TPA axis by $a_{\text{CAM}}/2$). The intermolecular and row separations are close to those observed for TPA on Au(111) (ref. 46).

The ordering of TPA on CAM, similar to that of TMA, is probably driven in part by a commensurability that arises from the near match of the period of CAM, a_{CAM} , and the expected⁴⁶ TPA molecular separation, a_{TPA} . We used molecular mechanics calculations to investigate the energetics of a single row that comprised 40 TPA molecules frozen in a configuration corresponding to the optimized gas-phase structure with an intermolecular separation of 0.977 nm (Fig. 5). The adsorption energy at different registries and positions was calculated, and our results show that the energy is reduced by about 0.09 eV per molecule when the row is aligned with the CAM lattice vectors (Fig. 5b and Supplementary Figs 6 and 7).

An energy map for different positions of a rigid, aligned row of TPA (Fig. 5d) shows that a minimum adsorption energy occurs when the TPA is adsorbed above CA. The contributions to the total energy from van der Waals and the electrostatic terms are also shown in Fig. 5d; as might be expected, we see minima in the van der Waals contribution when the TPA is above either a CA or a melamine molecule and a barrier region (0.1 eV per molecule) when the molecules are over voids in the CAM layer. This energy map indicates that the van der Waals contributions above the CA and melamine molecules are comparable. However, the Coulombic terms strongly favour adsorption above a CA molecule

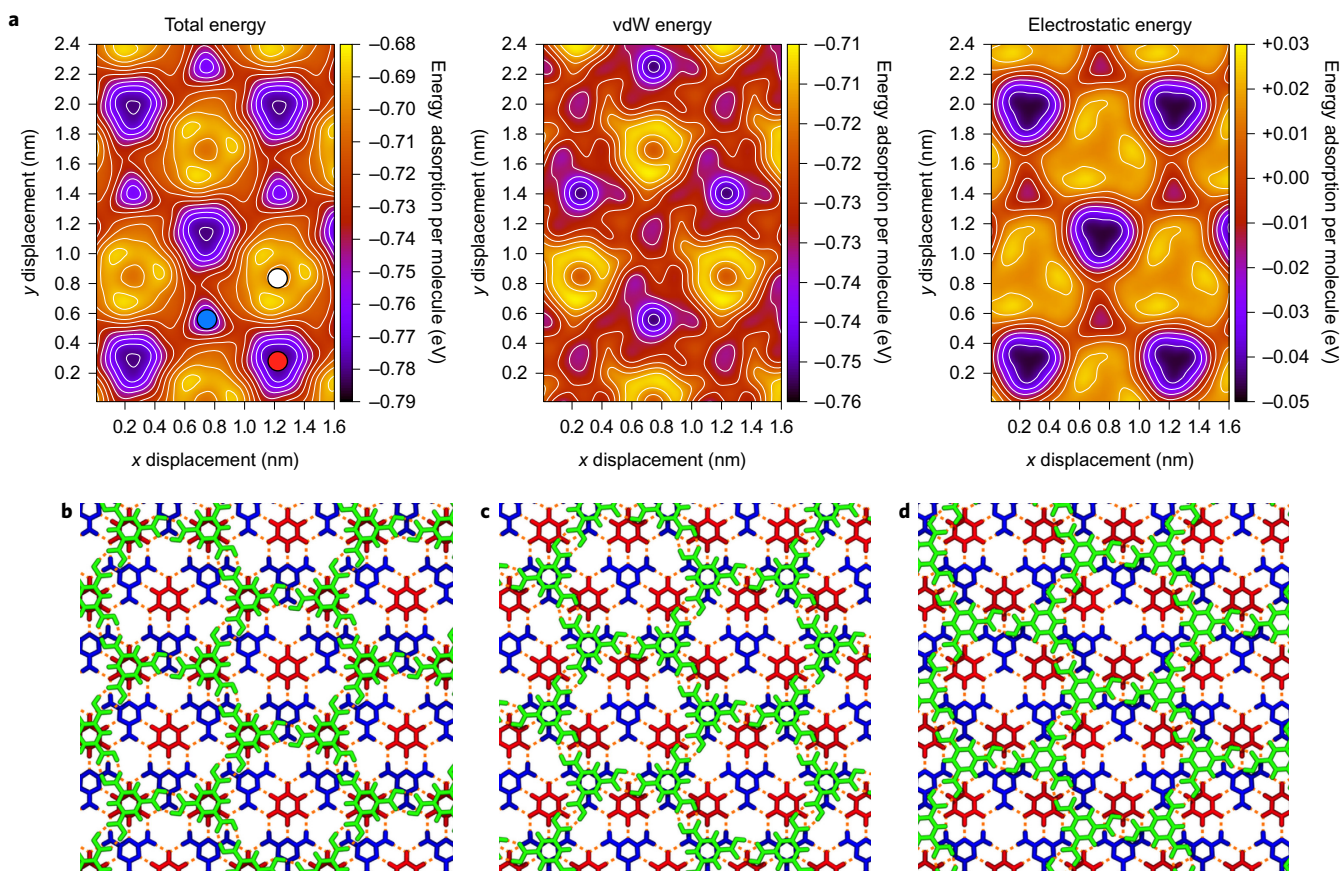


Figure 3 | Energetics of the CAM/TMA heterostructure. **a**, The lateral slide analysis of the total potential energy landscape for a TMA network as optimized in vacuum on CAM in the preferential mutual orientation (30°) shows the total energy (left), as well as the van der Waals (vdW, centre) and electrostatic (right) contributions to the energy as a function of the relative placement of the TMA layer over the CAM. **b–d**, Fully optimized TMA network that corresponds to the registries highlighted by the solid red (**b**), blue (**c**) and white (**d**) circles in **a**. The configurations in **b,c** correspond to a TMA sitting directly over a CA (**b**) or a melamine (**c**) molecule; these positions maximize the van der Waals contributions to the energy. In **d**, a TMA is directly over a void, which is an energetically unfavourable position. TMA, CA and MA are coloured in green, red and blue, respectively. Supplementary Figs 9–11 provide additional details and different orientations.

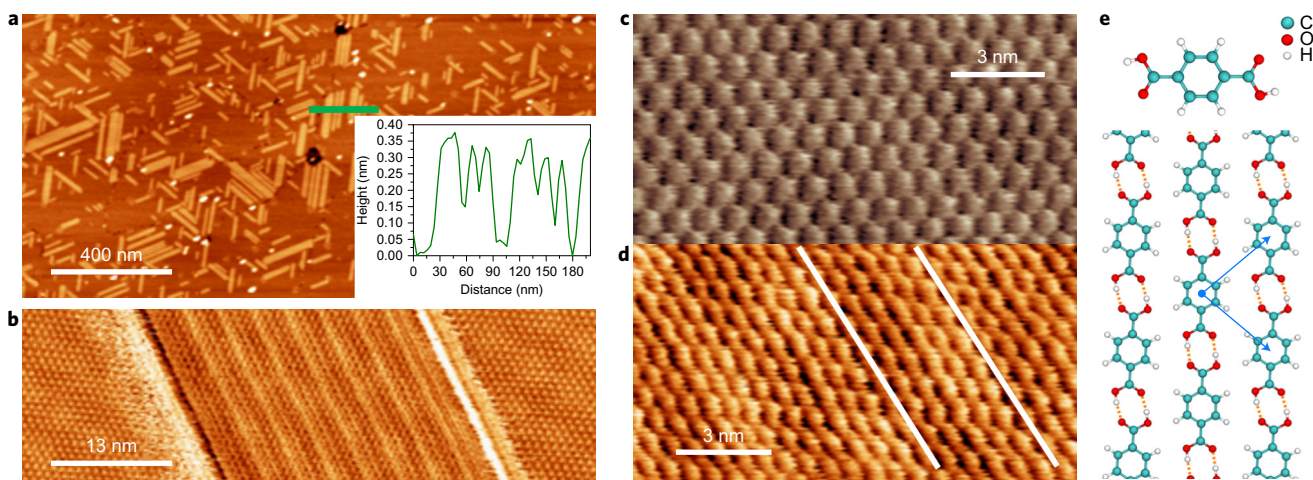


Figure 4 | TPA/CAM supramolecular heterostructure. **a**, The AFM image shows 1D crystallites of TPA adsorbed on a near-monolayer coverage of CAM. Inset: height profile along the green line. The topographic height of the island is approximately 0.3 nm, as expected for a monolayer. **b**, A phase image of a single TPA crystallite in which the TPA molecules, the underlying CAM network and the CAM/hBN moiré pattern can all be resolved. The alignment of the TPA rows with the principal axis of CAM is clearly resolved in this image. A contrast variation between TPA rows occurs because of a commensurability between CAM and TPA; the separation of bright rows is approximately 3.4 nm and corresponds to six rows. **c,d**, Contact mode images of the same area acquired at a low set point (**d**) in which the TPA rows are resolved, and at a higher deflection set point (**c**) in which the underlying CAM is revealed through the removal of the TPA; in combination, **c** and **d** show that every sixth TPA row is positioned over every fourth CAM row as highlighted by the white lines. **e**, Molecular structure of TPA (top), and TPA rows stabilized by hydrogen bonding (bottom) as optimized in vacuum. The lattice vectors of the TPA overlay are represented by blue arrows and correspond to $(a_{\text{CAM}}/\sqrt{3}, \pm a_{\text{CAM}}/2)$.

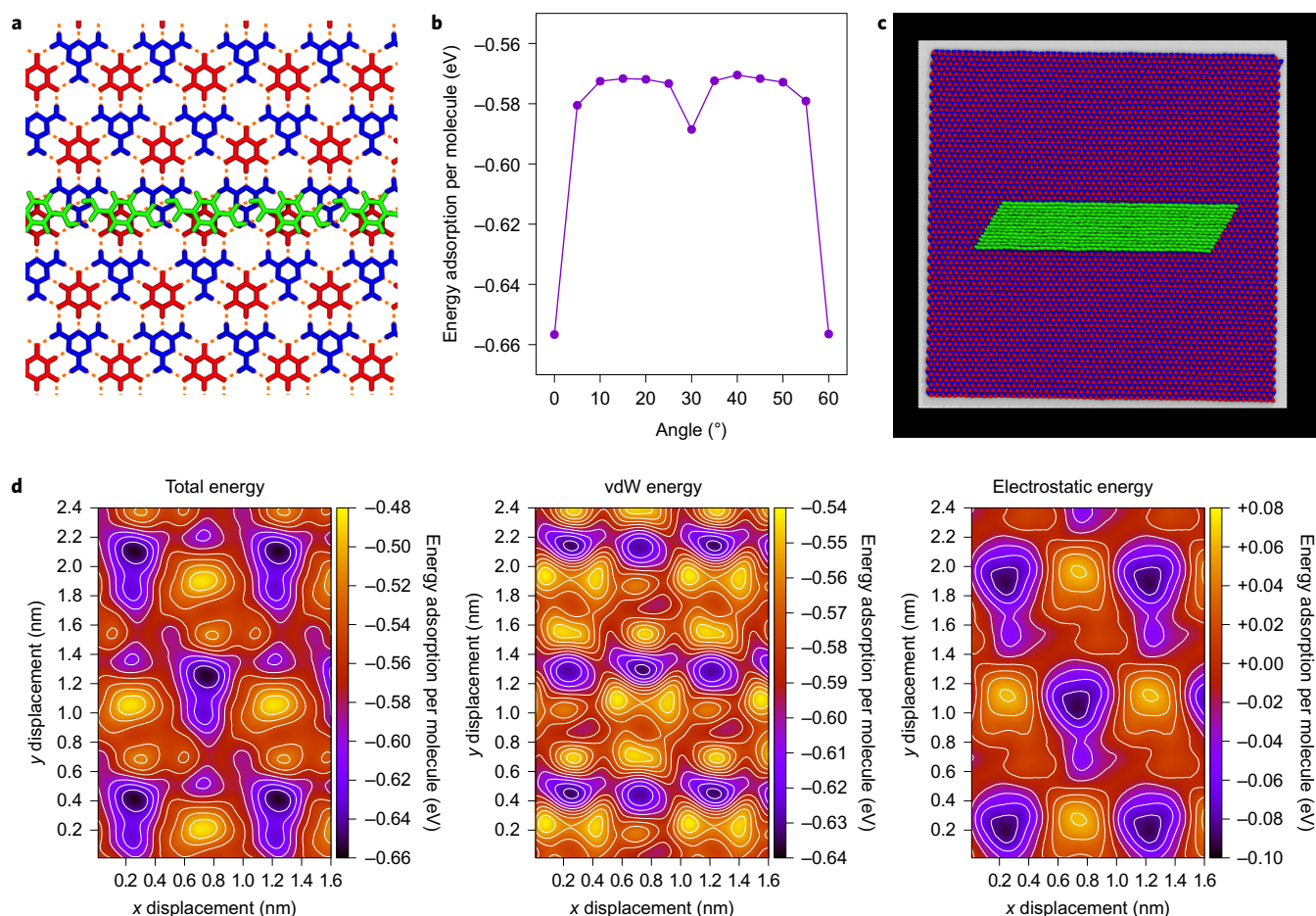


Figure 5 | Energetics of the CAM/TPA heterostructure. **a**, Fully optimized TPA row that corresponds to the global energy minimum. TMA, CA and MA are coloured in green, red and blue, respectively. **b**, Minimum of the adsorption energy as a function of the angle between the principal axis of the TPA row and the CAM lattice vector. **c**, A snapshot from MD simulations of 14 TPA rows on CAM/hBN in the preferential orientation. **d**, Lateral slide analysis of the total potential energy landscape (left) for a TPA row as optimized in vacuum on CAM in the preferential mutual orientation (0°), and the van der Waals (middle) and electrostatic energy (right) contributions. Supplementary Figs 6–8 provide additional details and different orientations.

and are calculated to be 0.18 eV per molecule lower above CA as compared with melamine. Similar energy plots are included in Supplementary Fig. 6 for rows in off-axis alignments. In addition, full relaxation for the TPA structures that correspond to the energy minima was performed and confirmed that these arrangements are thermodynamically stable. The low-energy regions near the minima extend to 0.2–0.4 nm in each direction, which allows for some flexibility in the positioning of TPA molecules on the CAM layer, which is important in the multirow systems.

The calculations of the energy of multiple parallel rows are more complex because the row separation does not match the periodicity of the CAM substrate. A large number of calculations for an arrangement of 14 rows, each containing 40 TPA molecules, with both different displacements between the TPA molecules in neighbouring rows and different inter-row separation was produced. Among those tested, arrangements with inter-row separation close to the experimental value (0.57 nm) give the lowest energy, for which the adsorption energy is -0.77 eV per molecule. The inter-row interaction provides an energy of -0.11 eV per molecule, and thus compensates the destabilization because some of the rows are not in the preferred adsorption sites. The stability of this configuration and the preferential alignment with the CAM layer is also confirmed by full MD simulations of the three-layered system (sample snapshots are shown in Fig. 5c and Supplementary Fig. 8). The relative displacement of neighbouring rows was more difficult to

capture, possibly because of an intrinsic limitation of the classical potential; several alternative models were explored, as described in Supplementary Information. Overall, there is good agreement between the computational predictions and our observations of both TMA and TPA alignment, periodicity and registry.

Our work demonstrates that supramolecular heterostructures can be formed by sequential deposition of layers with different structural and optical properties. For the systems studied here there is a well-defined epitaxial relationship between the grown layers and we can understand many of the observed properties using standard MD simulations. Although the interlayer interactions are dominated by van der Waals terms, which are not intrinsically directional, an orientational relationship emerges driven by the energy minimization that occurs with maximizing the interlayer close packing. Additional terms that arise from the Coulombic interactions determined by the relative positions of polar groups within the two layers are also significant in controlling the precise registry. There are therefore good prospects for predicting structural behaviour in analogue heterostructures between other materials.

In the future, we envisage that this approach to supramolecular heterostructures will provide the foundation for the growth of much more complex materials, in which multiple layers can be deposited sequentially with the possibilities to tune the chemical, optical and electronic properties of the resulting heterostructure. The exploitation of hydrogen bonding stabilizes the growth of 2D

sheets that have highly parallel interfaces. The use of hBN as a substrate suggests that this approach can be combined with 2D materials to introduce molecular functionality into stacked device architectures³², and may also provide a complete molecular analogue approach to the stacking of layered materials.

Methods

hBN flakes were mechanically exfoliated onto Si/SiO₂ substrates and briefly flame annealed prior to the adsorption experiments. CAM monolayers on hBN were prepared via adsorption from an 8 μM aqueous solution of melamine cyanurate. The melamine cyanurate solution was prepared from equal amounts of 8 μM solutions of melamine (99% (Sigma-Aldrich)) and CA (≥98% (Sigma-Aldrich)).

TMA was deposited on CAM from 20 μM and TPA from 60 μM ethanolic solutions. The adsorption time for TMA on CAM was 5 min and for TPA it was 20 min. The deposition was performed directly after the CAM complex was deposited on hBN flakes. After the deposition, the surface was blown dry with nitrogen for ~1 min. The samples were then immediately transferred to AFM for imaging.

AFM images were acquired with a Cypher AFM (Asylum Research Oxford Instruments) in both AC and contact modes using Multi75AI-G (Budget Sensor) cantilevers with a nominal spring constant of ~2.8 N m⁻¹ and a fundamental resonant frequency of ~75 kHz and higher harmonics of ~415 kHz (second harmonic) and ~1,280 kHz (third harmonic). We have also used NuNano Scout 350 probes with a nominal spring constant of 42 N m⁻¹ and resonant frequency of ~350 kHz (Nu Nano) and high-frequency Arrow UHF probes (NanoWorld) with a mean resonant frequency of ~2 MHz. All the imaging was performed in ambient conditions without any temperature or environmental control.

AFM images were analysed and extracted with WSxM software⁴⁷ (WSxM solutions).

Data availability. The authors declare that the data supporting the findings of this study are available within the article and its Supplementary Information files, or from the corresponding author on reasonable request. The AFM images from experiments on which this paper is based are also publicly accessible, free of charge, through Nottingham Research Data Management via <http://dx.doi.org/10.17639/nottingham.316>.

Received 22 February 2017; accepted 6 June 2017;
published online 24 July 2017

References

1. Elemans, J. A. A. W., Lei, S. & De Feyter, S. Molecular and supramolecular networks on surfaces: from two-dimensional crystal engineering to reactivity. *Angew. Chem. Int. Ed.* **48**, 7298–7333 (2009).
2. Macleod, J. M. & Rosei, F. Molecular self-assembly on graphene. *Small* **10**, 1038–1049 (2014).
3. Slater (née Phillips), A. G., Beton, P. H. & Champness, N. R. Two-dimensional supramolecular chemistry on surfaces. *Chem. Sci.* **2**, 1440–1448 (2011).
4. Wang, D., Wan, L.-J. & Bai, C.-L. Formation and structural transition of molecular self-assembly on solid surface investigated by scanning tunneling microscopy. *Mater. Sci. Eng. Rep.* **70**, 169–187 (2010).
5. Theobald, J. A., Oxtoby, N. S., Phillips, M. A., Champness, N. R. & Beton, P. H. Controlling molecular deposition and layer structure with supramolecular surface assemblies. *Nature* **424**, 1029–1031 (2003).
6. Baris, B. *et al.* Robust and open tailored supramolecular networks controlled by the template effect of a silicon surface. *Angew. Chem. Int. Ed.* **50**, 4094–4098 (2011).
7. Barth, J. V. *et al.* Building supramolecular nanostructures at surfaces by hydrogen bonding. *Angew. Chem. Int. Ed.* **39**, 1230–1234 (2000).
8. Barth, J. V., Costantini, G. & Kern, K. Engineering atomic and molecular nanostructures at surfaces. *Nature* **437**, 671–679 (2005).
9. Maier, S. *et al.* Nanoscale engineering of molecular porphyrin wires on insulating surfaces. *Small* **4**, 1115–1118 (2008).
10. Burke, S., Mativetsky, J., Hoffmann, R. & Grütter, P. Nucleation and submonolayer growth of C₆₀ on KBr. *Phys. Rev. Lett.* **94**, 096102 (2005).
11. Rahe, P. *et al.* Tuning molecular self-assembly on bulk insulator surfaces by anchoring of the organic building blocks. *Adv. Mater.* **25**, 3948–3956 (2013).
12. Li, B. *et al.* Self-assembled air-stable supramolecular porous networks on graphene. *ACS Nano* **7**, 10764–10772 (2013).
13. Korolkov, V. V. *et al.* Bimolecular porous supramolecular networks deposited from solution on layered materials: graphite, boron nitride and molybdenum disulphide. *Chem. Commun.* **50**, 8882–8885 (2014).
14. Korolkov, V. V. *et al.* Van der Waals-induced chromatic shifts in hydrogen-bonded two-dimensional porphyrin arrays on boron nitride. *ACS Nano* **9**, 10347–10355 (2015).
15. Ludwig, C., Gompf, B., Petersen, J., Strohmaier, R. & Eisenmenger, W. STM investigations of PTCDA and PTCDI on graphite and MoS₂. A systematic study of epitaxy and STM image contrast. *Z. Phys. B* **93**, 365–373 (1994).
16. Blunt, M. O. *et al.* Guest-induced growth of a surface-based supramolecular bilayer. *Nat. Chem.* **3**, 74–78 (2011).
17. Ciesielski, A. *et al.* Self-templating 2D supramolecular networks: a new avenue to reach control over a bilayer formation. *Nanoscale* **3**, 4125 (2011).
18. Xu, B., Tao, C., Cullen, W. G., Reutt-Robey, J. E. & Williams, E. D. Chiral symmetry breaking in two-dimensional C₆₀-ACA intermixed systems. *Nano Lett.* **5**, 2207–2211 (2005).
19. Wei, Y. & Reutt-Robey, J. E. Directed organization of C₇₀ kagome lattice by titanyl phthalocyanine monolayer template. *J. Am. Chem. Soc.* **133**, 15232–15235 (2011).
20. Skomski, D. & Tait, S. L. Interfacial organic layers for chemical stability and crystalline ordering of thiophene and carboxyl films on a metal surface. *J. Phys. Chem. C* **118**, 1594–1601 (2014).
21. Chen, W. *et al.* Orientationally ordered C₆₀ on *p*-sexiphenyl nanostripes on Ag (111). *ACS Nano* **2**, 693–698 (2008).
22. Huang, H. *et al.* Molecular orientation of CuPc thin films on C₆₀/Ag(111). *Appl. Phys. Lett.* **94**, 163303–163304 (2009).
23. Yoshimoto, S., Sawaguchi, T., Su, W., Jiang, J. & Kobayashi, N. Superstructure formation and rearrangement in the adlayer of a rare-earth-metal triple-decker sandwich complex at the electrochemical interface. *Angew. Chem. Int. Ed.* **46**, 1071–1074 (2007).
24. Yoshimoto, S. *et al.* Controlled molecular orientation in an adlayer of a supramolecular assembly consisting of an open-cage C₆₀ derivative and Zn^{II} octaethylporphyrin on Au(111). *Angew. Chem. Int. Ed.* **43**, 3044–3047 (2004).
25. Hinderhofer, A. & Schreiber, F. Organic-organic heterostructures: concepts and applications. *ChemPhysChem* **13**, 628–643 (2012).
26. Forster, R. *et al.* Electronic decoupling of aromatic molecules from a metal by an atomically thin organic spacer. *Adv. Mater.* **20**, 4450–4454 (2008).
27. Gruenewald, M. *et al.* Commensurism at electronically weakly interacting phthalocyanine/PTCDA heterointerfaces. *Phys. Rev. B* **91**, 155432 (2015).
28. Chen, W., Qi, D. C., Huang, H., Gao, X. & Wee, A. T. S. Organic-organic heterojunction interfaces: effect of molecular orientation. *Adv. Funct. Mater.* **21**, 410–424 (2011).
29. Schmitz-Hübsch, T. *et al.* Direct observation of organic-organic heteroepitaxy: perylenetetra-carboxylic-dianhydride on hexa-peri-benzocoronene on highly ordered pyrolytic graphite. *Surf. Sci.* **445**, 358–367 (2000).
30. Schwarze, M. *et al.* Band structure engineering in organic semiconductors. *Science* **352**, 1446–1449 (2016).
31. Orton, J. & Foxon, T. *Molecular Beam Epitaxy: A Short History* (Oxford Univ. Press, 2015).
32. Geim, A. K. & Grigorieva, I. V. Van der Waals heterostructures. *Nature* **499**, 419–425 (2013).
33. Perdigão, L. M. A., Champness, N. R. & Beton, P. H. Surface self-assembly of the cyanuric acid-melamine hydrogen bonded network. *Chem. Commun.* **28**, 538–540 (2006).
34. Zhang, X., Chen, T., Chen, Q., Wang, L. & Wan, L.-J. Self-assembly and aggregation of melamine and melamine-uric/cyanuric acid investigated by STM and AFM on solid surfaces. *Phys. Chem. Chem. Phys.* **11**, 7708–7712 (2009).
35. Staniec, P. A., Perdigão, L. M. A., Rogers, B. L., Champness, N. R. & Beton, P. H. Honeycomb networks and chiral superstructures formed by cyanuric acid and melamine on Au(111). *J. Phys. Chem. C* **111**, 886–893 (2007).
36. Xu, W. *et al.* Cyanuric acid and melamine on Au(111): structure and energetics of hydrogen-bonded networks. *Small* **3**, 854–858 (2007).
37. Ranganathan, A., Pedireddi, V. R. & Rao, C. N. R. Hydrothermal synthesis of organic channel structures: 1:1 hydrogen-bonded adducts of melamine with cyanuric and trithiocyanuric acids. *J. Am. Chem. Soc.* **121**, 1752–1753 (1999).
38. Griessl, S., Lackingner, M., Edelwirth, M., Hietschold, M. & Heckl, W. M. Self-assembled two-dimensional molecular host-guest architectures from trimesic acid. *Single Mol.* **3**, 25–31 (2002).
39. Plimpton, S. Fast parallel algorithms for short-range molecular dynamics. *J. Comput. Phys.* **117**, 1–19 (1995).
40. Jorgensen, W. L. & Tirado-Rives, J. The OPLS [optimized potentials for liquid simulations] potential functions for proteins, energy minimizations for crystals of cyclic peptides and crambin. *J. Am. Chem. Soc.* **110**, 1657–1666 (1988).
41. Jorgensen, W. L., Maxwell, D. S. & Tirado-Rives, J. Development and testing of the OPLS All-Atom Force Field on conformational energetics and properties of organic liquids. *J. Am. Chem. Soc.* **118**, 11225–11236 (1996).
42. Kannappan, K., Werblowsky, T. L., Rim, K. T., Berne, B. J. & Flynn, G. W. An experimental and theoretical study of the formation of nanostructures of self-assembled cyanuric acid through hydrogen bond networks on graphite. *J. Phys. Chem. B* **111**, 6634–6642 (2007).
43. Conti, S. & Cecchini, M. Accurate and efficient calculation of the desorption energy of small molecules from graphene. *J. Phys. Chem. C* **119**, 1867–1879 (2015).
44. Hutter, J., Iannuzzi, M., Schiffmann, F. & Van de Vondele, J. Cp2k: atomistic simulations of condensed matter systems. *Wiley Interdiscip. Rev. Comput. Mol. Sci.* **4**, 15–25 (2014).
45. Lee, J. H. A study on a boron-nitride nanotube as a gigahertz oscillator. *J. Korean Phys. Soc.* **49**, 172–176 (2006).

46. Clair, S. *et al.* STM study of terephthalic acid self-assembly on Au(111): hydrogen-bonded sheets on an inhomogeneous substrate. *J. Phys. Chem. B* **108**, 14585–14590 (2004).
47. Horcas, I. *et al.* WSXM: a software for scanning probe microscopy and a tool for nanotechnology. *Rev. Sci. Instrum.* **78**, 013705 (2007).

Acknowledgements

We are grateful to the Leverhulme Trust for providing financial support under grant RPG-2016-104 and to the Engineering and Physical Sciences Research Council for support through grant EP/N033906/1. E.B. gratefully acknowledges the receipt of a European Research Council Consolidator Grant; M.B. and E.B. acknowledge the University of Nottingham and Midplus High Performance Computing facilities for providing computational time. K.W. and T.T. acknowledge support from the Elemental Strategy Initiative conducted by MEXT, Japan, and the Japan Society for the Promotion of Science KAKENHI Grant Numbers JP26248061, JP15K21722 and JP25106006.

Author contributions

V.V.K. and P.H.B. conceived and designed the experiments, which were carried out by V.V.K. The hBN crystals were grown by K.W. and T.T. The numerical calculations were conceived through a discussion between M.B., E.B., P.H.B. and V.V.K., and were carried out by M.B. with additional input from E.B. The paper was written by P.H.B., V.V.K., M.B. and E.B. with revisions and comments from all of the authors.

Additional information

Supplementary information is available in the [online version of the paper](#). Reprints and permissions information is available online at www.nature.com/reprints. Publisher's note: Springer Nature remains neutral with regard to jurisdictional claims in published maps and institutional affiliations. Correspondence and requests for materials should be addressed to E.B. and P.H.B.

Competing financial interests

The authors declare no competing financial interests.